Geophys. J. Int. (1991) **106**, 53–65

A 2-D synthetic study of global traveltime tomography

Olafur Gudmundsson* and Robert W. Clayton
Seismological Laboratory, California Institute of Technology, Pasadena, CA 91125, USA

Accepted 1991 January 15. Received 1990 September 10

SUMMARY

A 2-D synthetic test study of global traveltime inversion for deep seated earth structure has been undertaken. This was done by generating traveltime residual data using reasonable models for earth structure. The data were then inverted by similar methods to those applied in global studies of earth structure. Our results indicate that models of the aspherical structure in the lower mantle based on traveltime data are only partially successful and only at the largest scales (harmonic degree ≤ 3) and that maps of the core–mantle boundary based on traveltimes are unsuccessful.

Key words: earth structure, inversion, traveltimes.

INTRODUCTION

The International Seismological Centre (ISC) Catalogue contains over 20 years of worldwide, arrival-time readings and event locations. This database of more than nine million picks has been used to map the heterogeneous structure of the earth's deep interior on a global scale. Clayton & Comer (1983) and Dziewonski (1984) used 15 years of ISC mantle *P*-wave data to map the lower mantle. Creager & Jordan (1986), Gudmundsson, Clayton & Anderson (1986), and Morelli & Dziewonski (1987) used compressional core phases to map the core–mantle boundary. Morelli, Dziewonski & Woodhouse (1986) and Shearer, Toy & Orcutt (1988), used *PKIKP*-waves to map anisotropy in the inner core. These studies, if successful, together with surface wave tomography, free-oscillation studies, and long-period, body wave synthesis, can provide important constraints on the style and scale of mantle convection, on the mechanisms of the geodynamo, and on the evolution of the earth.

There are, however, some concerns about the ISC data. The uncertainty of measurement is high compared with the signal attributable to aspherical structure. The data are contaminated by potentially systematic errors that are due to misidentification of phases, earthquake mislocation, earthquake time-function complexity, and potentially biased picking. The geometrical distribution of the data is uneven, because of the clustering of seismic sources in tectonically active regions, the lack of recording stations in the oceans, and the inactive picking of many secondary phases at numerous stations. The images may suffer from complex artifacts, which depend on the particular technique employed, because of the uneven coverage. The strong small-scale velocity variations in the earth's outermost layers are simplistically accounted for by station corrections. The severity of these problems is currently poorly understood.

We attempt in this paper to assess the quality of images of the lower mantle and core–mantle boundary (CMB) obtained from ISC data, by a synthetic test. In order to do that we need reasonable heterogeneous velocity models for the mantle as well as estimates of errors in the data. We draw our information from the results of crustal scattering studies (e.g., Aki 1973), from the results of surface wave tomography (upper mantle) (e.g., Woodhouse & Dziewonski 1984; Tanimoto 1987, 1988, 1990), from previous lower mantle body wave studies [i.e., Clayton & Comer (1983) (see also Hager & Clayton 1989), and Dziewonski (1984)] (hereafter referred to as CC and DZ, respectively), and from the results of Gudmundsson, Davies & Clayton (1990), for errors and statistical measures of the structure.

METHOD

The earth is a 3-D object containing 3-D heterogeneity. To address the potential problems of lower mantle traveltime studies fully, the full 3-D problem should be treated. This entails a great volume of computation in order to include small-scale structure in the crust and upper mantle, and because of the vast number of individual observations over the globe. We thus reduce the problem size by taking a sample, 2-D great-circle cross-section of the earth. Our choice of cross-section is shown in Figs 1 and 2 together with the distributions of events and stations used. Its normal vector is given by 45° N latitude and 135° E longitude. This great circle crosses two continents, one with abundant station coverage (North America), the other with sparse station coverage (Africa). The continents cover about 30 per cent of the great circle. It crosses two subduction zones, one

* Now at: University of Iceland Science Institute, Dunhaga 5, 107 Reykjavik, Iceland.

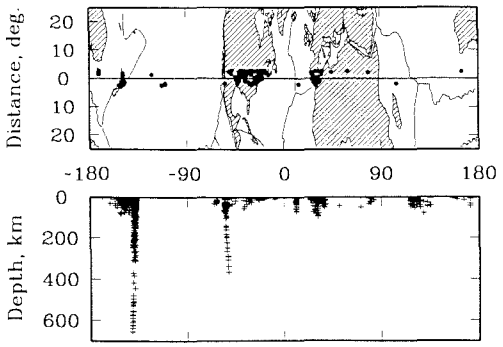

Figure 1. The distribution of stations (upper) and events (lower) used in synthetic case 1 (C1). The stations are selected from the ISC catalogue within a distance of 2.5° from the great circle drawn in the top frame. The events are selected in the same manner from the ISC catalogue, except that events are added in the two subduction zones (Tonga/New Zealand and Mexico/North America) to mimic the depth distribution of events in the entire ISC catalogue.

major and deep (Fiji–Tonga), the other minor and shallow (Mexico). It crosses two mid-ocean ridges, the North Atlantic ridge and the Indian Ocean ridge. The sparseness of recording stations and seismicity in the Pacific and Indian Oceans mimics the sparseness of sampling of the southern hemisphere of the globe in the 3-D case.

It is impossible to design a 2-D sample cross-section of the earth that is strictly analogous to the full 3-D problem. The aspects of the distribution of structure and data that one would like to mimic are as follows.

(1) The overall redundancy in the data relative to the characteristic scales of the structure.

(2) The redundancy in the data relative to the number of model parameters.

(3) The clustering characteristics of the data.

(4) The biases in the geometrical data distribution relative to strong structural features in the earth.

(5) The characteristic scale and strength of earth structure as it varies with depth.

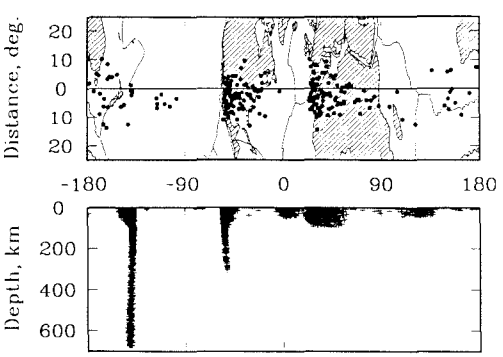

Figure 2. The distribution of stations (upper) and events (lower) used in synthetic case 2 (C2). Both distributions are artificial and constructed to mimic (a) the depth distribution of events in the ISC catalogue, (b) the lateral distribution of events and stations among a partition of the earth's surface into tectonic provinces, (c) the clustering characteristics of station and events in the ISC catalogue. Stations are given a random distribution about the reference great circle for plotting purposes only.

We infer the characteristics of earth structure from current models for the crust and upper and lower mantle. We constructed two case examples of the geometrical distribution of data. Case 1 (C1) is based on the ISC data in the vicinity of the above specified, sample great circle, but is lacking in the level of redundancy relative to the parametrization of the models we solve for. Case 2 (C2) is a completely artificial distribution of stations and events, but has comparable levels of redundancy in terms of numbers of data relative to numbers of model parameters, to the 3-D problems solved by CC and DZ.

The station distribution in case C1, shown in Fig. 1, was constructed by including all stations reporting more than 50 picks to the ISC catalogue between 1964 and 1986, which are within 2.5° from the great circle. We then added five stations to fill in uncharacteristically big gaps in the distribution. This yields 164 stations.

The seismicity distribution in case C1, also shown in Fig. 1, was constructed by including all the events reported to the ISC between 1964 and 1986 by at least 50 stations, which are within 2.5° from the great circle. We then define Benioff–Wadati zones as linear features at Tonga (New Zealand) and Mexico and collapse the seismicity in their vicinity onto them (4/5) and in the back arc region (1/5). The Benioff–Wadati zones are given finite widths (100–300 km) and the events are distributed normally (Gaussian distribution laterally) within them. We then added events at depth in both subduction zones to mimic the depth distribution of seismicity according to the ISC catalogue. The artificial subduction zones inserted into the distribution are not meant to resemble the actual zones the great circle crosses, but to mimic typical subduction zones. The number of events in this distribution is 1024.

If the geometrical distribution of data in the ISC catalogue were uniform, model space were cubic, and the model parametrization isotropic, the 3-D problem would scale to 2-D by taking the 2/3 root of the number of data. This is the criterion we used to determine the number of data in case C1. We selected the desired number of picks randomly, assigning probabilities proportional to the number of picks in the ISC catalogue for each event and station included in this case. The resulting number of picks is about 26 000.

Figure 2 shows the distribution of stations and events in case C2. We divided the great circle into tectonic provinces (subduction, tectonic, midocean ridges, intraplate). The sizes of the provinces were determined such that the proportion of the great-circle length categorized by a given tectonic type was the same as the proportion of the earth's surface area categorized as that same type. We then assigned earthquake loci at random within the tectonic provinces according to the relative numbers of events within each tectonic province type in the ISC catalogue. The depth was assigned at random such that the ISC depth distribution for the given tectonic type in the ISC catalogue was satisfied. The lateral position was assigned at random according to a Gaussian distribution around the axes of subduction zones and mid-ocean ridges, but a uniform distribution was assigned in tectonic and intraplate regions. The stations were selected at random from uniform deviates in oceanic intraplate regions, not at all at mid-ocean ridges, from uniform deviates in tectonic and subduction regions,

and from a decaying distribution on the continents away from adjacent tectonic or subduction zones.

The total number of events and stations was selected such that the reduction from the number of events and stations in the ISC catalogue was approximately the square root of the reduction of the number of generated picks from the number of picks in the ISC catalogue. The number of *P*-wave picks was determined in this case such that the ratio of picks to model parameters is the same as in the case of CC for analogous model parametrization. The picks were distributed among the station–event pairs that fall in any given epicentral distance window such that the epicentral distance distribution in the ISC data was satisfied. The number of stations, events, and picks in this case is 245, 4981, and 120 000, respectively.

Table 1 shows a count of the number of picks of some of the compressional phases reported to the ISC between 1964 and 1986, as well as the number of stations and events with more than 50 picks in the same period. No windowing of crossovers of traveltime branches, or selection according to maximum traveltime residual has been applied. The *P* data include everything between epicentral distances of 25° and 95°. *PKPbc* picks are counted, assuming that 85 per cent of all *PKP* picks between distances of 143° and 154° are *PKPbc* (Anderssen & Cleary 1980). The remaining 15 per cent are counted as *PKPdf*. Numbers of stations, events, and picks of all the compressional phases used in this study in both synthetic cases (C1 and C2) are also given in Table 1.

A heterogeneous earth model was constructed from three basic models. Model UML is a model of large-scale slowness variations in the upper mantle. Model UMS is a model of small-scale slowness variations in the crust and upper mantle. Model LM is a model of slowness variations in the lower mantle.

Shallow heterogeneity in the earth is known to correlate well with surface tectonics on large scales and thus the distribution of data in the ISC catalogue. There is therefore potential for the bias of lower mantle models from shallow heterogeneity. The best global models of shallow heterogeneity come from surface wave tomography (e.g., Woodhouse & Dziewonski 1984; Tanimoto 1987, 1988). These studies are primarily sensitive to shear velocity variations. We took the DSXRG model of Tanimoto (1988) as the basis for our UML model. For a Poisson solid with correlated velocity variations (*S*- and *P*-wave), traveltime residuals scale with slowness perturbations. Observations of the ratio of *S*- to *P*-wave station corrections are generally close to 4 s (e.g., Hales & Doyle 1967; Souriau & Woodhouse 1985), although Romanowicz & Cara (1980) suggest that this high ratio may be an artifact for USA stations. To convert the DSXRG model to a viable compressional velocity model, we thus scaled it by a factor of 1/4 in terms of slowness. We took the same great-circle cross-section of the model as was used in constructing the event and station distributions in case C1 (see Fig. 1).

To include the effects of slabs, we inserted slab-like anomalies at Tonga (New Zealand) and Mexico, that coincide with the Benioff–Wadati zones in the data distribution. These anomalies are Gaussian in the lateral dimension of widths 100–300 km and have a maximum strength of relative velocity variation of 5 per cent. This is in accord with seismic studies of slab structure (Mitronovas & Isacks 1971; Suyehiro & Sacks 1979) and thermal modelling of slabs (e.g., Schubert, Yuen & Turcotte 1975; Creager & Jordan 1984). The width was increased linearly with depth, and the relative strength decreased linearly with depth to 2.5 per cent. We also inserted spherical, Gaussian, slow anomalies in the back-arc regions at a depth of 200 km with a radius of 100 km and maximum strength of 2.5 per cent. These structures are similar to features in the Hellenic model of Spakman, Wortel & Vlaar (1988). These slab features are not large scale in the lateral dimension, but they are strong structural features, which correlate with the data distribution. Model DSXRG of Tanimoto (1988) includes harmonic degrees up to 8. The results of Gudmundsson *et al.* (1990) indicate that above a depth of 400 km significant power extends beyond that scale. Given those results we added randomly selected harmonic components to model UML according to a Gaussian decay of the power spectrum with a half-width of 10–15 harmonic degrees. The resulting model, UML, is plotted in Fig. 3(a). The structure near the Tonga slab is highlighted in Fig. 3(b). The imposed spectral decay beyond harmonic degree 8 is shown in Fig. 3(c).

Model UMS is meant to describe the small-scale structure of the upper mantle. Localized scattering studies at dense arrays (e.g., NORSAR and LASA) indicate that in the top 150 km of the earth the small-scale velocity structure is characterized by 5 per cent variations on a characteristic scale of 10 km (e.g., Aki 1973). The results of Gudmundsson *et al.* (1990) are consistent with this. We took those results for the variation of small-scale power with depth in the upper mantle, assumed a correlation length of 10 km and constructed the UMS model accordingly (see Fig. 4). This was done by parametrizing the model at a 10 km scale and selecting incoherent random numbers for the model parameters from a Gaussian distribution with standard deviation as a function of depth according to Fig. 4.

Global models of slowness heterogeneity in the lower mantle agree to within a factor of 2 on the rms (root-mean-square) level of heterogeneity. The models of CC, DZ, Tanimoto (1990) (*S* velocity), and Gudmundsson *et al.* (1990) agree on an rms low in the central lower mantle and an increase towards both the core–mantle boundary (CMB) and the upper mantle. These studies are also consistent with a characteristic scale-length of heterogeneity throughout much of the lower mantle of the order of 1000 km. We took the results from Gudmundsson *et al.* (1990) for the power and correlation length of slowness variations in the lower mantle and constructed a model

Table 1. Numbers of events, stations, and picks of various phases in the ISC catalogue (1964–1986) and the two synthetic cases set up in this study. I refers to C1, II to C2.

	ISC	C1	C2
stations	1650	164	245
events	25000	1024	4981
P-picks	3000000	26024	120000
P-srays	100000	987	3671
PcP-picks	35000	1331	1327
PKPab-picks	20000	941	734
PKPbc-picks	400000	4677	15509
PKPdf-picks	500000	6356	16493

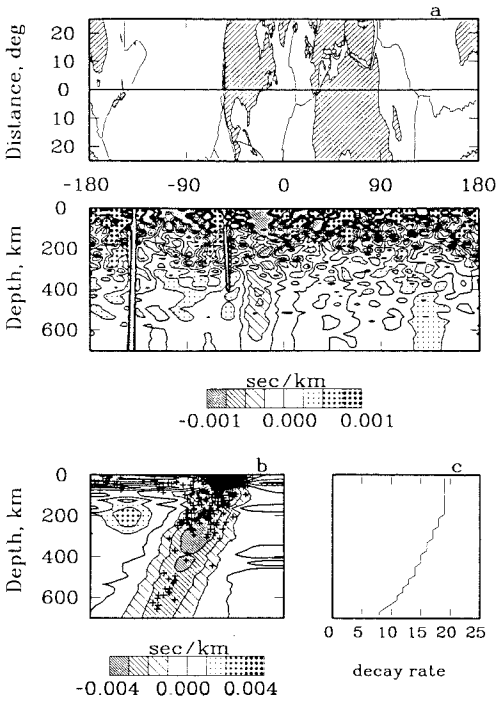

Figure 3. The large-scale, upper mantle model (UML) used for both C1 and C2. It was constructed from a great-circle cross-section of model DSXRG of Tanimoto (1988). This shear velocity model was scaled by a factor of one-quarter in terms of slowness. We then inserted artificial slab structures into it (at New Zealand and Mexico), and finally, appended the power spectrum of the model according to the decay rates presented in (c), given here as the harmonic-degree half-width of the spectrum. (b) shows an enlargement of the New Zealand subduction zone and its seismicity.

accordingly. The construction was done by generating an incoherent random field at a parametrization interval of 1° (60–100 km). We then convolved that field with a Gaussian function of width varying with depth according to the specified correlation length. Power was then adjusted according to the results of Gudmundsson *et al.* (1990) depth layer by layer. The resulting model, LM, is shown in Fig. 5(a). The variation of correlation length with depth is shown in Fig. 5(b), and the variation of the rms level of heterogeneity with depth in Fig. 5(c).

We used the spherically symmetric, reference velocity

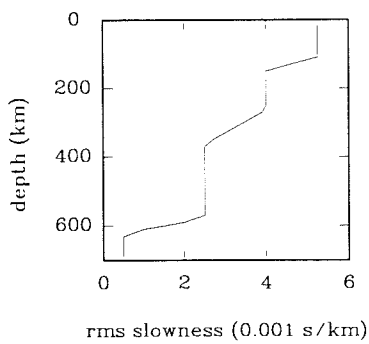

Figure 4. The small-scale upper mantle model (UMS) used in both C1 and C2. It was constructed by a random process yielding a model of 10 km correlation length and rms level as a function of depth as shown here.

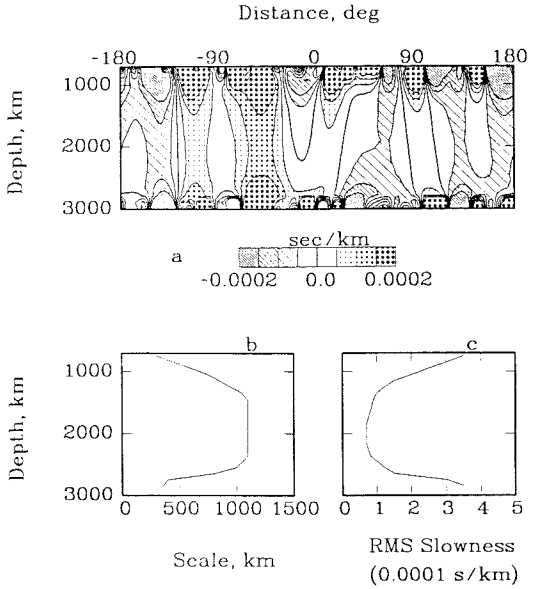

Figure 5. The lower mantle model (LM) used for both C1 and C2. (a) A contour map of the model. (b) The variation of correlation length with depth. (c) The variation of the rms level of the model as a function of depth. The model was constructed by an incoherent, random, number generator, then smoothed according to (b), and, finally, the amplitude was adjusted according to (c).

model of Jeffreys and Bullen (JB) (Jeffreys 1939) and power-law ray tracing (see Bullen 1979) to construct ray geometries. The above models were densely parametrized by small constant value cells and they integrated along the rays according to the linearized, ray-theoretical, traveltime integral:

$$\delta t = \delta u(\mathbf{x})\, dS(\mathbf{x}), \tag{1}$$

where δt is the traveltime residual, δu stands for slowness perturbations, dS for path length along the ray, and $\mathbf{x}$ is a position vector.

Finally, we took the estimates of error in the ISC *P*-wave data from Gudmundsson *et al.* (1990) (Fig. 6) and added to the data randomly generated numbers accordingly. The data then consist of four distinct contributions: from models UML, UMS, LM, and from random errors. The variances of the individual contributions to all the data are shown in Tables 2 and 3 for cases C1 and C2, respectively. The two

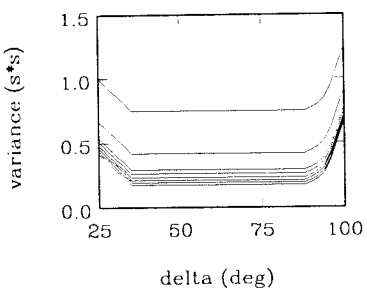

Figure 6. The variation of random-error variance with epicentral distance and source depth for the *P*-wave data. The different curves represent different source depths, with the highest variance for shallow events, and the variance monotonically decreasing with source depth. The eight curves are 100 km increments in depth.

Table 2. Variances of the various contributions to the different data sets constructed in synthetic case C1. UML represents contributions from the upper mantle UML model. UMS stands for contributions from the upper mantle UMS model. LM stands for contributions from the lower mantle LM model. ERR stands for contributions from random errors. TOTAL refers to the total variance of each data set prior to relocations or static corrections.

phase	UML	UMS	LM	ERR	TOTAL
P	0.82	0.20	0.24	0.72	2.11
PcP	0.96	0.14	0.16	0.87	2.03
PKPab	0.49	0.12	0.38	0.94	1.99
PKPbc	0.53	0.13	0.06	0.93	1.73
PKPdf	0.78	0.12	0.14	0.87	2.08

tables are similar except for the difference in UML contributions to the *PKPab* and *PKPbc* data sets. This could be coincidental, as the relative distribution of these data to the UML model is quite different.

The ISC traveltime residuals are given relative to the JB model and event locations made by the ISC with teleseismic compressional data (mantle *P*-waves and *PKIKP*-waves). Some studies have referenced the traveltime data to the PREM model and appropriately relocated the events. The use of teleseismic data to locate events can introduce significant errors in location because of small-scale lateral structure, particularly around the event, that may introduce spatially systematic errors in the traveltime residuals. We therefore relocate all events laterally, based on the synthetic data that we compute, based on what are exact locations. The initial location is the exact location. We relocate only laterally, because of the unresolved trade-off of origin time and source depth, because of the use of teleseismic data only. We use our synthetic data sets for *P*-waves and *PKIKP*-waves in the relocation (these are the first arrivals at almost all distance ranges). The results of the relocation are shown in Fig. 7 for both cases (C1 and C2). The patterns of relocations are quite similar for the two cases, largest for the subduction events, and of the order of 20 km where largest. This is similar to the results of Mitronovas & Isacks (1971), Engdahl, Sleep & Lin (1977), and Fujita, Engdahl & Sleep (1981) for real subduction-zone events. A 10 km relocation introduces an error of up to the order of 1 s (mantle velocity is of the order of 10 km s^{-1}).

The next step in the data processing was applying static station and event corrections, using the method of CC. This was done by an iterative scheme, where first the average residual for each event is explained by an event correction, then having corrected the data for the event correction, the average residual of each station is attributed to a station correction and removed. This cycle is repeated until convergence is reached. The event correction is roughly

Table 3. Same as Table 2 for case C2.

phase	UML	UMS	LM	ERR	TOTAL
P	0.90	0.22	0.34	0.63	2.21
PcP	0.87	0.15	0.21	0.86	1.98
PKPab	1.10	0.13	0.20	0.96	2.33
PKPbc	1.13	0.14	0.16	0.84	2.22
PKPdf	0.96	0.14	0.19	0.84	2.21

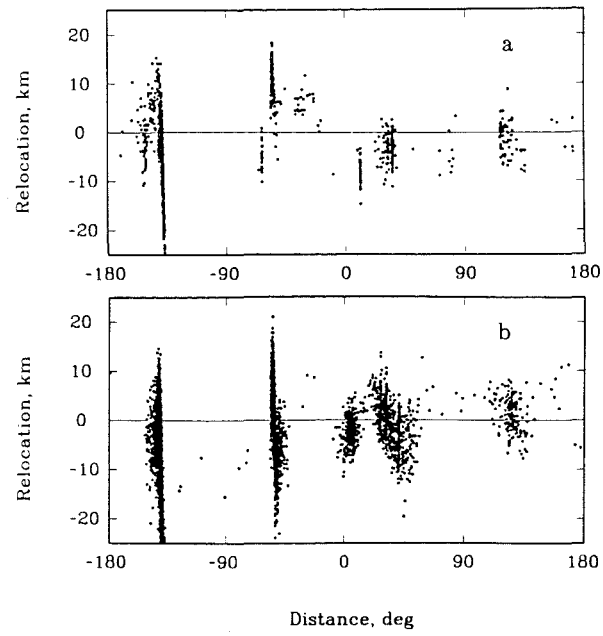

Figure 7. The results of lateral relocations of the events (a) used in C1, (b) used in C2. The relocation is 1-D and plotted in km. The sign indicates whether the events were relocated clockwise or counterclockwise.

equivalent to relocation in depth and origin time. The results of the statics are shown in Fig. 8 in the same format as the relocation results. Fig. 8(a) shows the individual station statics in case C1 as a function of position along the great circle; Fig. 8(b) shows the event static corrections in case C1 as a function of great-circle position; Fig. 8(c) shows the station statics in case C2, and Fig. 8(d) the C2 event statics. Event statics are generally negative in the Tonga subduction zone, particularly within the slab, and in the Mexican subduction zone event statics are negative relative to a positive regional trend. The Mexican subduction zone is immersed in a regional slow anomaly. The patterns of event and station statics are similar for both cases C1 and C2. The shallow fast anomaly under North America is associated with negative event and station statics. The shallow, slow anomaly under the western margin of North America coincides with positive station and event statics. The positive corrections in the eastern Atlantic and African region are due to an overall slow upper mantle. Thus the static corrections correlate well with the strongest features of model UML. This is what one hopes for, as the statics are the simplistic way lower mantle, traveltime studies typically attempt to account for upper mantle structure.

The last step in the data processing was the formulation of summary rays (see, e.g., Dziewsonki 1984). In order to reduce the volume of the inverse problem and to give regions at the earth's surface a more equal weight in the inversion for lower mantle structure, previous studies have applied the summary-ray concept. The earth's surface is divided into patches of uniform size, and all rays with endpoints within common patches are lumped together. Those rays have similar travel paths through the lower mantle (and core) and thus sample deep, large-scale anomalies similarly. They may pick up a variable signal from small-scale, shallow structure, which will cancel. Further-

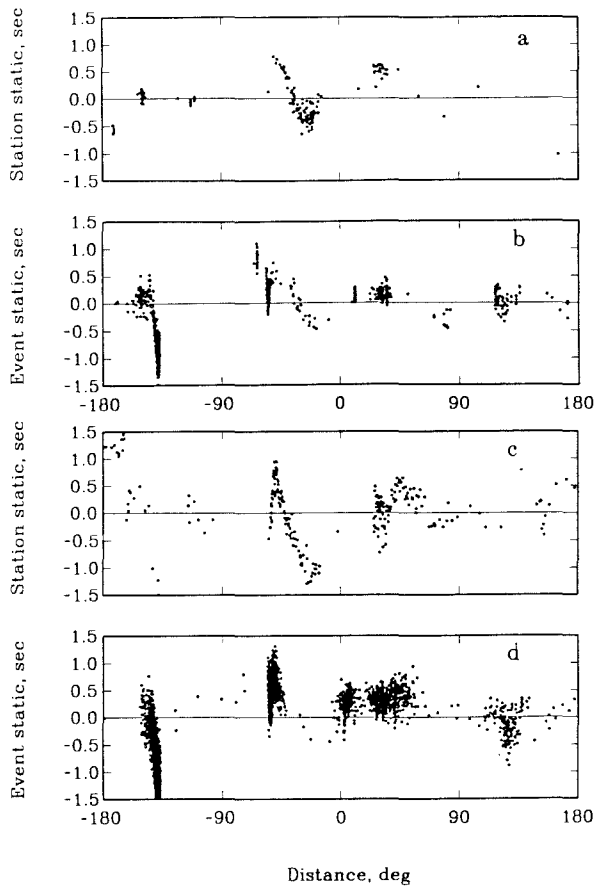

Figure 8. Event and station static corrections (a) and (b) for case C1, (c) and (d) for case C2. Both are plotted in seconds and against position along the reference great circle. Note the similarities between the two cases and the correlation with the main features of model UML.

more, if a large number of rays pass through a shallow seated anomaly, its effect is given reduced weight by collapsing all the rays into a single summary ray. The density of coverage in the lower mantle is evened. We applied summary rays at a scale of 5° in case C2 as did CC and DZ, but at a scale of 2.5° in case C1 in order to adjust the level of redundancy (relative number of summary-ray data and model parameters). The number of summary rays for *P*-waves was 760 and 3670 for cases C1 and C2, respectively.

Finally, we inverted our processed, synthetic *P*-wave data sets for structure in the lower mantle, using similar procedures to those applied by CC and DZ. This involves two significantly different inversion techniques (which yield significantly different results). The technique of DZ expands the model in terms of a small number of continuous, orthonormal basis functions and applies a standard least-squares method to solve for the coefficients of each function. The functions used are the five lowest order Legendre polynomials in depth and the seven lowest degree spherical harmonics laterally. We will hereafter refer to this technique as THE (truncated harmonic expansion). The technique of CC divides the model into discrete boxlike cells, assumes a constant slowness perturbation within each cell, and applies an iterative back-projection inversion

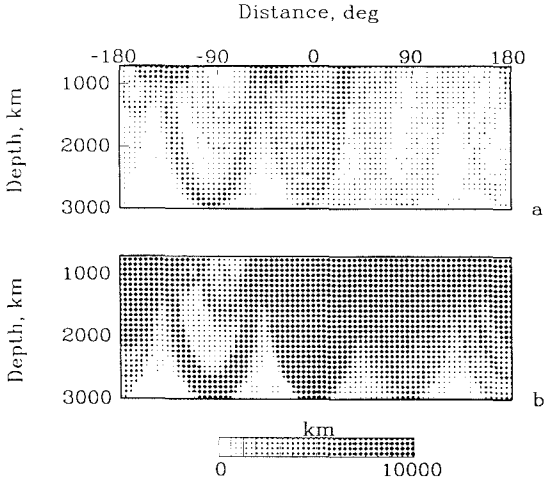

Figure 9. Hitcounts in the lower mantle (a) for C1, (b) for C2. Here hitcount is presented in terms of the total path length within each model cell in the discrete parametrization of the BP method.

scheme to solve for a large number of model parameters. We will hereafter refer to this technique as BP (back-projection). Our adaptation of the THE method uses five Legendre polynomials to expand the depth variation and a truncated (at degree 6) discrete Fourier transform to expand the lateral variation (spherical harmonics in the plane of the equator). This level of parametrization is equivalent to that used by DZ for the 3-D earth. The level of parametrization in the BP method is also kept equivalent to that used by CC. The binning interval in depth is 100 km and in the lateral dimension is 5°. The damping parameter used in the application of the BP method is 50 km, or the same used by CC in their global inversion. In applying the BP method we used data from all source depths, while in applying the THE method we used only data from shallow events (depth <50 km). All comparisons of the results of the two methods and with the LM model are done with equally parametrized models. The THE parametrization is the sparsest one. The BP and LM models (finely discrete) were expanded *a posteriori,* out to degree 10 and using eight depth polynomials, by a least-squares fit. Only those parameters equivalent to those used in THE are included.

Figure 9 shows the ray coverage in the lower mantle in cases C1 and C2 in terms of the total ray path length within each model cell in the BP parametrization. The coverage is considerably better in the C2 case, since the total number of summary rays is about 5 times greater. The coverage is relatively poor at the base of the mantle in both cases. Rays from Tongan events to American stations give an illusion of reasonable coverage under the Pacific. However, this densely covered path is not crossed by many other paths.

RESULTS

The results of the inversion of the *P*-wave data set, which includes all contributions of signal and error, by both the BP and THE methods are shown in Figs 10 and 11 for cases C1 and C2, respectively. The centre frame shows the LM model for reference. The contouring is the same for all models. It is clear from these figures that the success of the inversion is

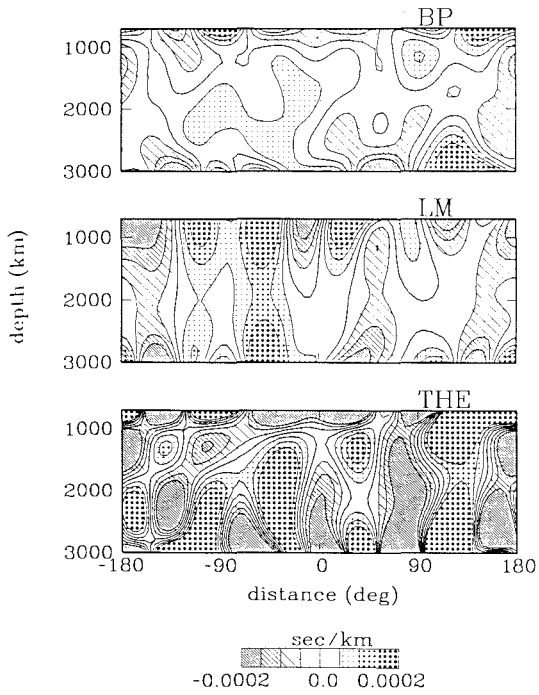

Figure 10. The result of inversion for structure in the lower mantle by the BP and THE methods for case C1. The LM model is plotted for reference.

marginal. The BP model is lacking in power at the top of the lower mantle relative to LM in both cases C1 and C2. The THE model has excessive power throughout the lower mantle relative to LM in both cases. The visual correlation of the models is reasonable at best and poor at the top and bottom, particularly in case C1. Figs 12–15 show the

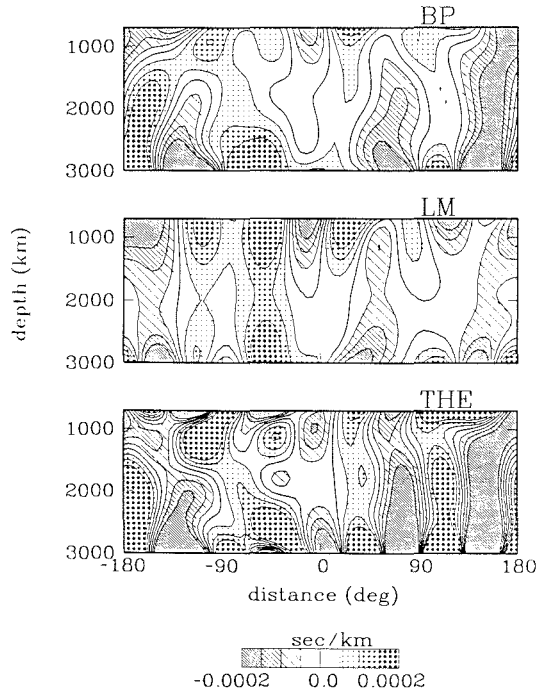

Figure 11. The result of inversion for structure in the lower mantle by the BP and THE methods for case C2. The LM model is plotted for reference.

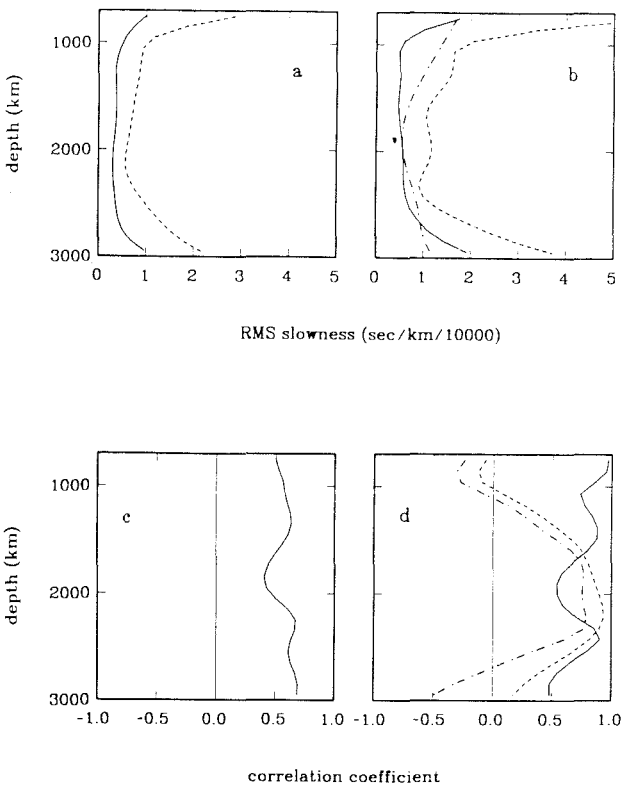

Figure 12. The variation of the rms level of slowness anomalies and correlation coefficient as functions of depth in the lower mantle for case C1. Harmonic degrees 1–3 are included. In (a) we plot the rms level of models CC (solid line) and DZ (dashed line). In (c) we plot the correlation coefficient of models CC and DZ. In (b) the solid line represents the BP model, the dashed line the THE model and the doubly dashed line the LM model. In (d) the solid line is the correlation between BP and THE, the dashed line the correlation between BP and LM and the doubly dashed line the correlation between THE and LM.

standard deviation (root-mean-square anomaly) of the models and their depth by depth correlation. Analogous parameters for the 3-D results of CC (model CC) and DZ (model DZ) are shown for reference. Fig. 12 includes harmonic degrees 1, 2 and 3 and shows the results in case C1. The behaviour of the rms slowness is similar for the 2-D synthetic case and the 3-D case. The DZ model is consistently about a factor of 2 higher in amplitude than the CC model and the THE model is about a factor of 2 larger than model BP. The power in model BP falls closer to the power of model LM than does the power of model THE.

Models CC and DZ correlate consistently positively at this parametrization, but at a relatively low level of 0.6. The correlation of models BP and THE is also consistently positive and somewhat higher (0.7). However, each of the models correlates significantly worse with the LM model. In particular, the correlation goes to zero or negative values at the top and bottom of the lower mantle. Fig. 13 shows harmonic degrees 1–6 of the results from case C1. The behaviour of rms slowness is still similar for the 2-D and 3-D cases. The amplitude discrepancy between THE and BP is in this case magnified over the discrepancy between DZ and CC. The correlation of CC and DZ on one hand, and BP and THE on the other is still positive overall and somewhat

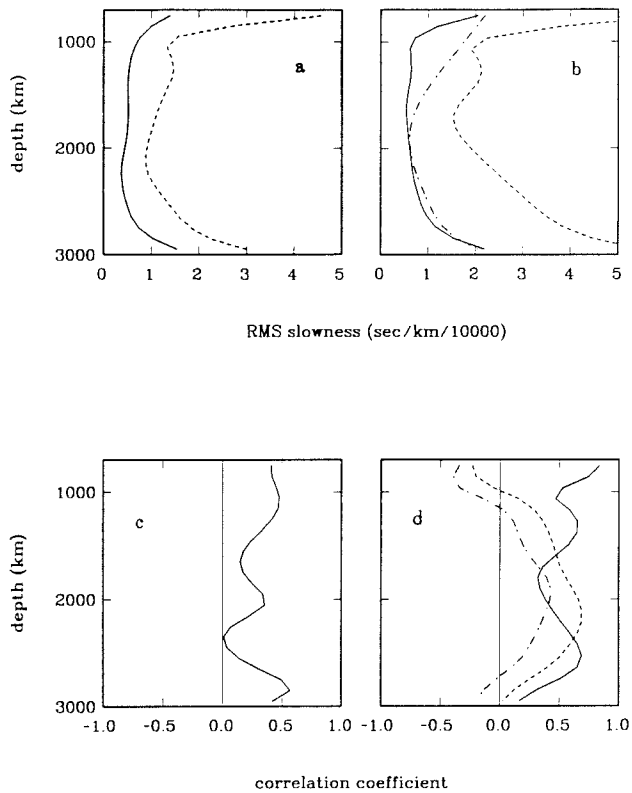

Figure 13. Same as Fig. 12 with harmonic degrees 1–6 included.

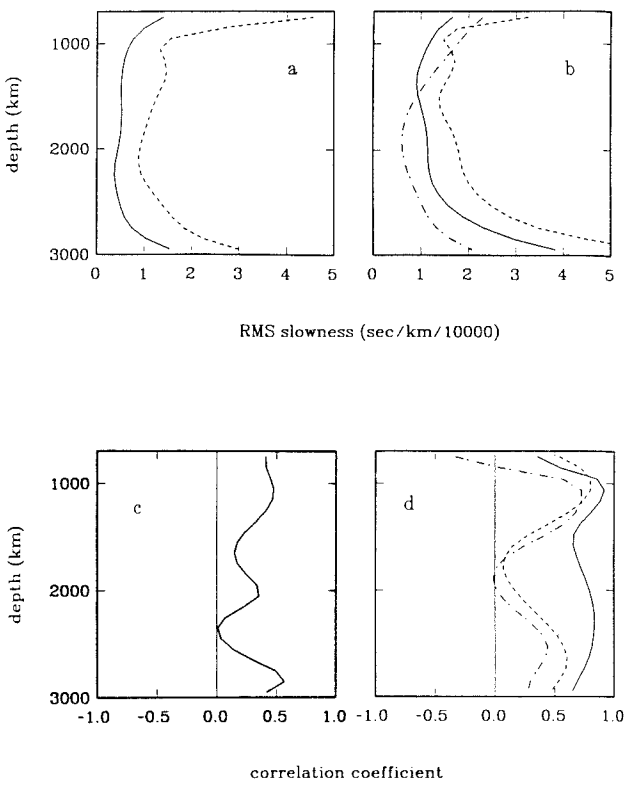

Figure 15. Same as Fig. 12 for case C2 with degrees 1–6 included.

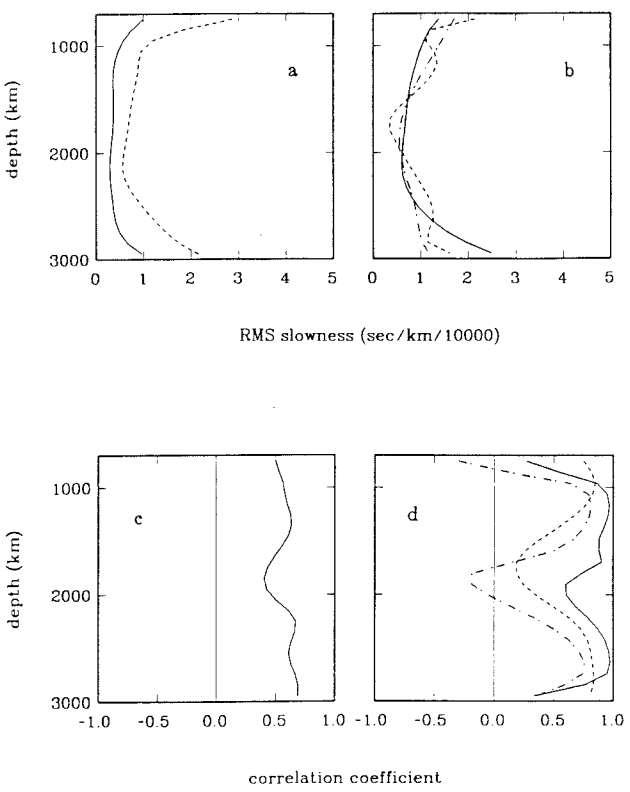

Figure 14. Same as Fig. 12 for case C2 with degrees 1–3 included.

higher in the latter case. Fig. 14 shows degrees 1, 2, and 3 for case C2. In this case the rms slowness is similar for all of LM, BP, and THE. The correlation of BP and THE is very high throughout much of the lower mantle, drops towards the top and bottom and drops slightly in the lower mantle. The correlation of models BP and THE with LM is in this case low in the centre of the lower mantle and remains positive at the top and bottom, while dropping somewhat. Fig. 15 shows degrees 1–6 of the results from case C2. Here the amplitude discrepancy between BP and THE reappears, but in the lower part of the lower mantle both models overestimate the rms slowness of the LM models significantly. The correlation of THE and BP is similar to Fig. 14, only slightly reduced. The higher correlation of BP and the THE than CC and DZ in both cases C1 and C2 may be an indication that the problems with the data are underestimated in this 2-D synthetic example. Bear in mind, however, that the 3-D expansion up to degree 6 involves 49 parameters, while the 2-D expansion up to degree 6 involves only 12. The lower the number of parameters the more likely random components in the field correlate. This discrepancy may be a manifestation of this number effect.

The BP model correlates significantly better with the LM model than does the THE model. This may be due to the lower level of parametrization, i.e., aliasing, or that in the application of the THE method we used only shallow events ($Z < 50$ km), as did DZ. Shallow data are more evenly distributed than deep data, but contain larger random errors (see Gudmundsson *et al.* 1990) and pick up a higher contribution from upper mantle structure. On the other hand, deep events may be more likely to be poorly located

because of the strong lateral velocity anomalies of subducting slabs.

We can apply a significance test to the correlation coefficient. The correlation coefficient of two N-long strings of numbers taken from the same Gaussian distribution follows a distribution that approaches a Gaussian distribution at high N. The standard deviation of this distribution behaves as the inverse square root of N. Thus, we calculate that the overall correlation of models CC and DZ for harmonic degrees 1–3 and 1–6 is about two standard deviations. The probability that this correlation is coincidental is very low (2.5 per cent). We calculate that the correlation of models BP and THE is about 1.7 standard deviations in case C1 and about 2.0 standard deviations in case C2. The probability that this correlation is coincidental is about 4.5 and 2.5 per cent, respectively. Thus, the lower correlation in the 3-D case is actually more significant than the higher correlation in the 2-D C1 case and about as significant as the correlation is the 2-D C2 case. In both cases the correlation is highly significant. That is not necessarily to say that the non-coincidental cause of the correlation is lower mantle structure. In fact, the poorer correlation of the BP and THE models with LM than with each other implies that it is not so. The problem evidently lies in the data values rather than in their spatial distribution.

To estimate the effect of the lack of coverage in the lower mantle on the resolution of this problem, we tried inverting data containing contributions from the lower mantle only (no upper mantle, no errors). The correlations of the results of that inversion are shown in Fig. 16 (case C1, harmonic degrees 1–6). The correlation is nearly perfect down to a few hundred km above the CBM. This demonstrates that the data spatially resolve the lower mantle structure at the present parametrization.

Figures 17 and 18 show the rms amplitude (left column) and correlation with LM of models obtained by the BP method from various combinations of the individual contributions to the data for cases C1 and C2, respectively. The top pairs of frames are the same as in Figs 13 and 15. The lower four pairs are from data excluding one or more

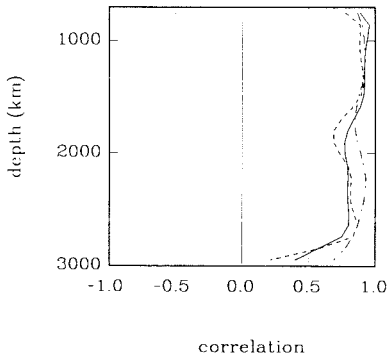

Figure 16. The correlation of the LM model with models computed by the BP and THE methods from data generated from the LM model only. (No upper mantle structure, no errors, no relocations, no statics.) The solid line is the correlation of models BP and THE, the dashed line the correlation between models BP and LM, and the doubly dashed line the correlation between models THE and LM.

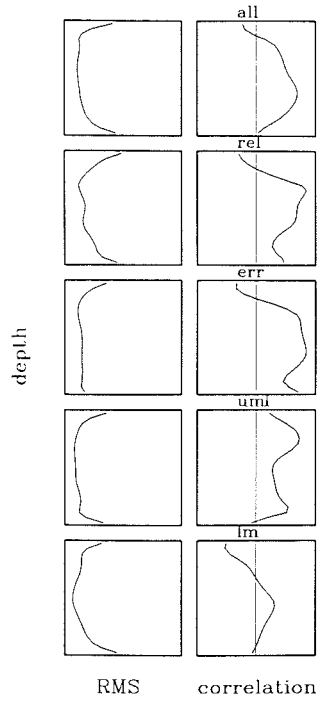

Figure 17. Rms slowness variations and correlation with the LM model for the results of BP inversions of various data sets in case C1. Harmonic degrees 1–6 are included. 'All' refers to data including all contributions; 'rel' refers to data excluding event relocations; 'err' refers to data with random errors excluded; 'uml' refers to data with contributions from the UML model excluded; 'lm' refers to data with contributions from the LM model excluded. Scales are the same as in Figs 13–16.

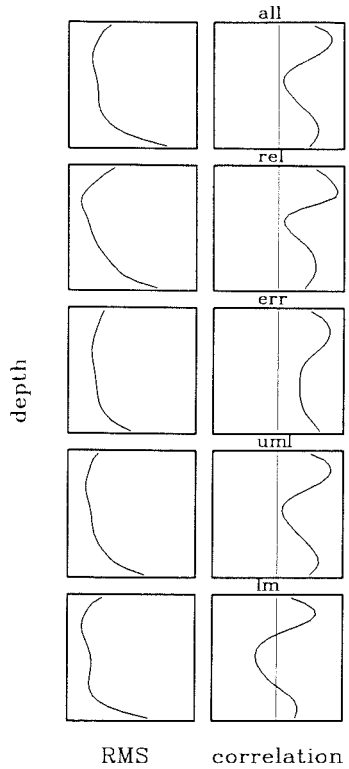

Figure 18. Same as Fig. 17 for case C2.

contributions as indicated. REL refers to data excluding relocation errors. Here little is changed at the top of the model, but the correlation is significantly improved at depth in the C1 case. The correlation is somewhat improved in case C2. ERR refers to data excluding random errors and contributions from small-scale, upper mantle structure. Again the effect is small at the top of the model, but is much improved at depth in case C1 and at central lower mantle depths in case C2. The correlation a few hundred km above the CMB is reduced in case C2 but increased at the very base of the mantle. A common effect of excluding random errors is the reduction in the rms amplitude at the base of the mantle for both cases C1 and C2. This implies that the increase in power at the base of the mantle may be at least in part due to a combination of poor coverage there and large errors in the data. UML refers to data excluding contributions from the UML model. In case C1 the correlation is improved at the top of the lower mantle, but reduced at central depths. There is remarkably little effect in case C2. LM refers to data excluding contributions from the lower mantle. The correlation is low, but significantly negative at the top and positive at central depths in case C1. In case C2 this is reversed. This indicates that in these particular synthetic cases the geometrical distribution of data and upper mantle structure are such that pervasive effects manifest themselves throughout the mantle. In case C1 the positive correlation in the LM case at central depths is consistent with the reduced correlation in the UML case from ALL. The depth profile of correlation in the C2-LM case is quite similar to that of C2-ALL, except for a constant shift. This constant shift of about 0.3 may be a better measure of the correlation between the BP model and the LM model, which is actually due to the signal from the LM model. Note how little effect the exclusion of the various components of the data has on the rms amplitude depth profiles. The only notable difference appears to be the effect of random errors on rms amplitude at the base of the mantle. The overall differences between cases C1 and C2 are only slight. The variation of rms amplitude is similar for the two cases, despite a factor of 5 difference in overall redundancy. The behaviour of correlation with depth is quite different in the two cases, while the overall level of correlation is similar. This points at the sensitivity of the artifacts of these inversions to the specifics of the distribution of data and its relation to the structure, and indicates the need for a full-fledged 3-D synthetic test of global, traveltime tomography.

Figures 19 and 20 show the results of inverting for CMB structure using the various core data sets. The data were generated using the same upper and lower mantle structures as the *P*-wave data, the same relocation errors, but estimates of random error obtained by a stochastic approach similar to that applied by Gudmundsson *et al.* (1990), yielding error variance of about 1 s for all of the core data sets. The core data contain no contribution from the CMB or below it. Each frame represents the result for one particular phase. The bottom frame shows the result from a simultaneous inversion of all the phases, with all summary rays given equal weights. The inversion technique used was damped least squares. The model parametrization in the inversion included harmonic degrees up to and including degree 8, and the inversion solves for the harmonic

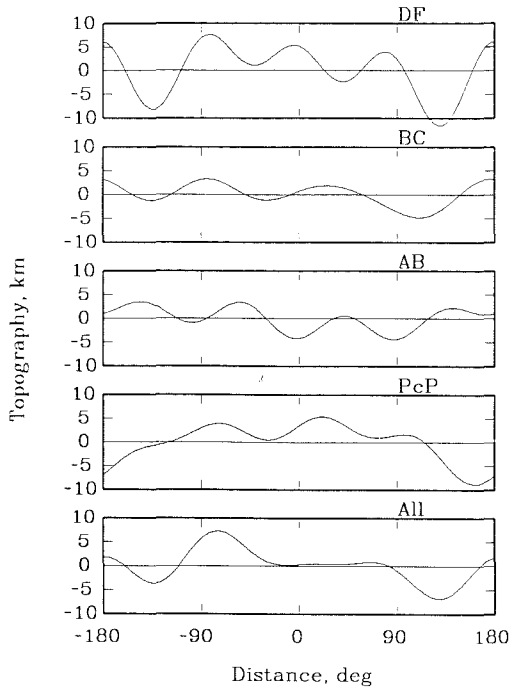

Figure 19. Topography of the CMB (degrees 1–4) from inversion of compressional, core-wave data sets as indicated. Case C1.

coefficients (Fourier coefficients) much like Morelli & Dziewonski (1987) did. The figures include only degrees 1–4. The overall peak-to-peak amplitude of these patterns is fairly consistently of the order of 10–20 km for all the phases, highest for *PKPdf* (*PKIKP*), despite the fact that this is the biggest data set. Also note that in general the topography is higher in case C2 than in C1, in spite of the

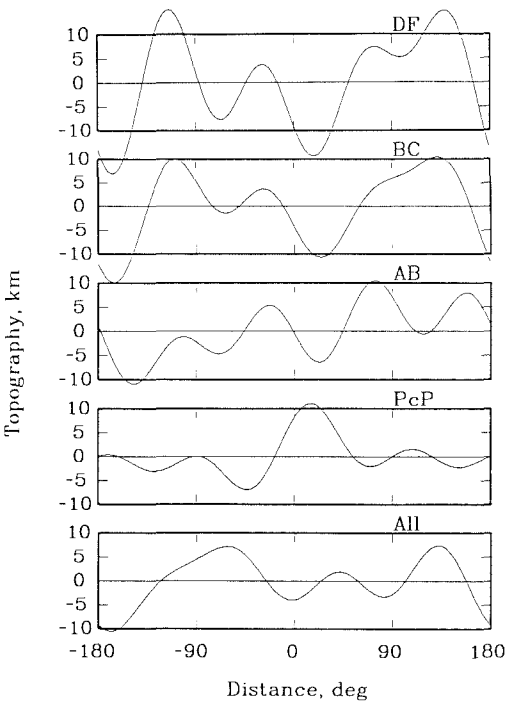

Figure 20. Topography of the CMB (degrees 1–4) from inversion of compressional, core-wave data sets as indicated. Case C2.

higher degree of redundancy in case C2. This implies that the uncertainty of models of the CMB obtained from ISC traveltime data is at this level of parametrization of the order 5–10 km, and that this uncertainty is less related to random errors in the data than to spatially coherent errors, such as relocation errors and upper mantle structure, that statics do not account for.

DISCUSSION AND CONCLUSIONS

The overall conclusion of this study is a negative one. Our results indicate that the usefulness of the ISC data for mapping the aspherical structure of the earth's deep interior is limited. It should be pointed out, however, that this kind of synthetic study is only as good as the information that goes into it. We have used a specific model of lateral velocity variations for the upper mantle, which we claim has a large detrimental effect on lower mantle inversion. How realistic is this model? We have used a specific model for the lower mantle. How realistic is it? Are our estimates of error reasonable? Is our modelling of event-location errors appropriate? We have simplified a 3-D problem to a 2-D problem. How would our conclusions be changed if we were able to set up a 3-D synthetic study? Are there any effects in the ISC data that we have left out? We think that our choices of inputs into this synthetic study stand to reason, but that a number of the parameters chosen should have the effect of underestimating problems of lower mantle, traveltime inversion.

A number of reports of surface wave tomographic studies have been published (e.g., Nakanishi & Anderson 1984; Woodhouse & Dziewonski 1984; Nataf, Nakanishi & Anderson 1986; Tanimoto 1987, 1988). These studies agree satisfactorily, although not impressively. Furthermore, they agree with regional, body wave synthesis studies (e.g., Helmberger, Engen & Grand 1985) and regional, tomographic studies using S-waves (Grand 1987). The level of large-scale, shear wave heterogeneity in the upper mantle is consistently estimated at about 5 per cent and the pattern consistently correlates with surface tectonics. As to the scaling of the shear wave model of Tanimoto (1988) to construct a realistic P-wave model, this is done on the basis of P/S-wave station correction ratios (e.g., Hales & Doyle 1967; Souriau & Woodhouse 1985). We take the value of 4, which is at the upper end of the range of values obtained by researchers. Using a smaller ratio would increase the strength of the upper mantle structure and make the problems introduced by it more severe. We extended the spectra of the model beyond degree 8 based on the results of Gudmundsson *et al.* (1990), but in a decaying manner and only out to about degree 15. We inserted slab structures into the model, but conservatively chose a maximum amplitude of the slab anomaly at 5 per cent. We dispersed the Benioff–Wadati seismicity throughout the several hundred km thick slab anomaly, whereas it could be more focused within the slab and thus cause larger event mislocations.

The model we used for the lower mantle was based on previous deterministic and stochastic studies of the lower mantle using the ISC data (CC, DZ, and Gudmundsson *et al.* 1990). As we have demonstrated in this study, these studies suffer from upper mantle contamination and random errors. Both problems could insert undue power into the models. We thus expect the amplitude of the lower mantle model to be too high rather than too low. Reducing its amplitude would effectively reduce the relative signal contribution from the lower mantle and thus serve to make the problems more severe.

The main source of errors in the data was assumed to be random in this study. There is reason to expect the ISC data to contain some level of spatially systematic errors that are due to phase mispicks, etc. Systematic errors do not cancel upon stacking as random errors do and thus more effectively obscure images obtained from the data. (We attempt to model the spatially coherent errors that are due to relocation errors in this study.)

The static event- and station-correction results in our 2-D synthetic tests (see Fig. 8) correlate well with the main structural features in the upper mantle model, UML. This is in general agreement with studies of station corrections from ISC data (e.g., Dziewonski & Anderson 1983). Our results for the lateral relocations of events (see Fig. 7) yield maximum relocations in slab regions of the order of 20 km. This is consistent with slab event-relocation studies (e.g., Fujita *et al.* 1981) and indicates that our modelling of location errors in the ISC data is reasonable.

We cannot make inferences about the possible differences between these 2-D synthetic test cases and a 3-D synthetic study based on the actual data geometry in the ISC catalogue. The extension of the spectra of model DSXRG did assume random phase to construct model UML. It is likely that at least some of the power in the upper mantle structure at degrees 10–15 is due to components that serve to sharpen the transitions between the larger scale anomalies and thus are correlated in phase. It is not clear what effect this might have on our results, although they are probably minor.

We argue above that the effects of upper mantle structure and data errors on lower mantle, traveltime inversion may be underestimated. The checks that we have to compare with the 3-D models of CC and DZ, namely, their correlation and amplitude as compared to the correlation and amplitude of our models BP and THE, are similar, however. The significance of the overall level of correlation is about the same in our 2-D synthetic cases as in the 3-D case. Furthermore, the amplitude depth profiles are similar, and the factor of 2 amplitude discrepancy between the two models is reproduced. Correlation of our inversion results with the input model, LM, is consistently positive in at least parts of the lower mantle. Inspection of Figs 10 and 11 shows that some of the input structures are successfully modelled. This indicates that lower mantle, traveltime inversions for aspherical structure are, in fact, partially successful.

Hager *et al.* (1985) presented comparisons between the large-scale geoid pattern and that predicted from the results of CC and DZ through a dynamic, mantle-flow model for a few, simple, mantle-rheology models. The comparison is impressive for harmonic degrees 2 and 3 and those rheology models that render the geoid largely insensitive to upper mantle structure and structure at the base of the mantle. The sensitivity kernels are in these cases negative throughout the lower mantle. Thus this comparison involves a large degree of smoothing in depth. It is because of this smoothing that the geoid patterns, that are predicted from

models CC and DZ, correlate much better than the analogous patterns in the models themselves. The same is likely to hold for the correlation of the predicted geoids with the observed (or residual) geoid versus the correlation of the structural models with the true structure of the lower mantle. In the results of our synthetic tests, the inversion results from both methods (BP and THE) correlate positively with the input model (LM) in the depth range where the geoid kernels are large. Thus a similar calculation to that of Hager *et al.* (1985) would yield similar results.

We attempt to discern the cause of the partial failure of the inversion results of the BP method to correlate with the input LM model in Figs 17 and 18. The interpretation of the figures is not clear: The effect of random errors appears to be significant and greater at depth in the models, where the level of redundancy in the ray coverage is generally less than at the top of the lower mantle. The same is true for the effect of relocations in case C1. In case C1 contamination from the upper mantle structure appears to be greatest at the top of the lower mantle. The insensitivity of the amplitude-versus-depth profiles to omitting components of the data (see Figs 17 and 18), including contributions from lower mantle structure, casts doubt on recent lower mantle results.

The amplitude ratio of the DZ and CC models is reproduced in THE and BP models. In case C1 the ratio is about the same at degrees 1, 2, and 3, but higher when degrees 4, 5, and 6 are included. In case C2 the ratio of THE to BP is close to unity for degrees 1, 2, and 3, but about 2 (same as DZ to CC) when degrees 4, 5, and 6 are included. In both cases the relative ratio increases at the higher degrees, which approach the truncation degree of THE and DZ. This may indicate that the excess power in the THE and DZ results is due to aliasing. In other words, power belonging to harmonic degrees that are not included in the model parametrization may leak into the model parameters corresponding to scales that are comparable to the truncation scale.

Our estimate of uncertainty of traveltime-based maps of the CMB is of the order of 5 or 10 km. This is about the peak-to-peak amplitude of recent studies of the CMB from traveltimes (e.g., Morelli & Dziewonski 1987). If this estimate is correct, recent results for the CMB are completely obscured.

In closing, we suggest on the basis of the present results, that while the ISC data have a reasonably high signal-to-noise ratio (including small-scale, structural signal in the signal) of the order of 2 for teleseismic *P*-waves (see Gudmundsson *et al.* 1990), and a good enough spatial distribution to resolve earth structure at the parametrization of say Dziewonski (1984) (see Fig. 16), greater care must be taken to account for shallow structure. We need good, detailed models for the strongly heterogeneous upper mantle and good locations for the events used.

ACKNOWLEDGMENTS

This work was supported by NSF awards EAR83-17623 and EAR83-51371. O.G. was supported by a fellowship from the Phillips Petroleum Company. Contribution no. 4890, from the Division of Geological and Planetary Sciences, Caltech.

REFERENCES

Aki, K., 1973. Scattering of P waves under the Montana Lasa, *J. geophys. Res.*, **78,** 1334–1346.

Anderssen, R. S. & Cleary, J. R., 1980. Estimation of PKP times from ISC data, *Phys. Earth planet. Inter.*, **23,** 207–214.

Bullen, K. E., 1979. *An Introduction to the Theory of Seismology*, 3rd edn, Cambridge University Press, Cambridge, UK.

Clayton, R. W. & Comer, R. P., 1983. A tomographic analysis of mantle heterogeneities from body-wave travel-times, *EOS, Trans. Am. geophys. Un.*, **64,** 776.

Creager, K. C. & Jordan, T. H., 1984. Slab penetration into the lower mantle, *J. geophys. Res.*, **89,** 3031–3049.

Creager, K. C. & Jordan, T. H., 1986. Aspherical structure of the core–mantle boundary from PKP travel times, *Geophys. Res. Lett.*, **13,** 1497–1500.

Dziewonski, A. M., 1984. Mapping the lower mantle: Determination of lateral heterogeneity in P velocity up to degree and order 6, *J. geophys. Res.*, **89,** 5929–5952.

Dziewonski, A. M. & Anderson, D. L., 1983. Travel times and station corrections for P waves at teleseismic distances, *J. geophys. Res.*, **88,** 3295–3314.

Engdahl, E. R., Sleep, N. H. & Lin, M. T., 1977. Plate effects in north Pacific subduction zones, *Tectonophysics*, **37,** 95–116.

Fujita, K., Engdahl, E. R. & Sleep, N. H., 1981. Subduction-zone calibration and teleseismic relocation of thrust-zone events in the central Aleutian Islands, *Bull. seism. Soc. Am.*, **71,** 1805–1828.

Grand, S. P., 1987. Tomographic inversion for shear velocity beneath the North American plate, *J. geophys. Res.*, **92,** 14 065–14 090.

Gudmundsson, O., Clayton, R. W. & Anderson, L., 1986. CMB topography inferred from ISC PcP travel times, *EOS, Trans. Am. geophys. Un.*, **67,** 1100.

Gudmundsson, O., Davies, J. H. & Clayton, R. W., 1990. Stochastic analysis of global travel-time data: Mantle heterogeneity and random errors in the ISC data, *Geophys. J. Int.*, **102,** 24–43.

Hager, B. H. & Clayton, R. W., 1989. Constraints on the structure of mantle convection using seismic observations, flow models, and the geoid, in *Mantle Dynamics*, ed. Peltier, W. R.

Hager, B. H., Clayton, R. W., Richards, M. A., Comer, R. P. & Dziewonski, A. M., 1985. Lower-mantle heterogeneity, dynamic topography and the geoid, *Nature*, **313,** 541–545.

Hales, A. L. & Doyle, H. A., 1967. *P* and *S* travel-time anomalies and their interpretation, *Geophys. J. R. astr. Soc.*, **13,** 403–415.

Helmberger, D. V., Engen, G. & Grand, S., 1985. Upper-mantle cross-section from California to Greenland, *J. geophys.*, **58,** 92–100.

Jeffreys, H., 1939. The times of P, S, and SKS and the velocities of P and S, *Mon. Not. R. astr. Soc., Geophys. Suppl.*, **4,** 498–533.

Mitronovas, E. & Isacks, B. L., 1971. Seismic-velocity anomalies in the upper mantle beneath the Tonga–Kermadec island arc, *J. geophys. Res.*, **76,** 7154–7180.

Morelli, A. & Dziewonski, A. M., 1987. Topography of the core–mantle boundary and lateral homogeneity of the liquid core, *Nature*, **325,** 678–683.

Morelli, A., Dziewonski, A. M. & Woodhouse, J. H., 1986. Anisotropy of the inner core inferred from PKIKP travel times, *Geophys. Res. Lett.*, **13,** 1545–1548.

Nakanishi, I. & Anderson, D. L., 1984. Measurements of mantle wave-velocities and inversion for lateral heterogeneity and anisotropy, 2. Analysis by the single-station method, *Geophys. J. R. astr. Soc.*, **78,** 573–617.

Nataf, H. H., Nakanishi, I. & Anderson, D. L., 1986. Measurements of mantle wave-velocities and inversion for

lateral heterogeneities and anisotropy 3. Inversion, *J. geophys. Res.*, **91,** 7261–7307.

Romanowicz, B. A. & Cara, M., 1980. Reconsideration of the relations between S and P station anomalies in North America, *Geophys. Res. Lett.*, **7,** 417–420.

Schubert, G., Yuen, D. A. & Turcotte, D. L., 1975. Role of phase transitions in a dynamic mantle, *Geophys. J. R. astr. Soc.*, **42,** 705–735.

Shearer, P. M., Toy, K. M. & Orcutt, J. A., 1988. Axi-symmetric Earth models and inner-core anisotropy, *Nature*, **333,** 228–232.

Souriau, A. & Woodhouse, J. H., 1985. A worldwide comparison of predicted S-wave delays from a three-dimensional upper-mantle model with P-wave station corrections, *Phys. Earth planet. Inter.*, **39,** 75–88.

Spakman, W., Wortel, M. J. R. & Vlaar, N. J., 1988. The Hellenic subduction zone: A tomographic image and its geodynamic implications, *Geophys. Res. Lett.*, **15,** 60–63.

Suyehiro, K. & Sacks, I. S., 1979. P- and S-wave velocity anomalies associated with the subducting lithosphere determined from travel-time residuals in the Japan region, *Bull. seism. Soc. Am.*, **69,** 97–114.

Tanimoto, T., 1987. The three-dimensional, shear-wave structure in the mantle by overtone waveform-inversion. I, Radial-seismogram inversion, *Geophys. J. R. astr. Soc.*, **89,** 713–740.

Tanimoto, T., 1988. The 3D shear-wave structure in the mantle by overtone waveform-inversion. II, Inversion of X-waves, R waves and G waves, *Geophys. J. R. astr. Soc.*, **93,** 321–333.

Tanimoto, T., 1990. Long-wavelength, S-wave velocity structure throughout the mantle, *Geophys. J. Int.*, **100,** 327–336.

Woodhouse, J. H. & Dziewonski, A. M., 1984. Mapping the upper mantle: Three-dimensional modeling of Earth structure by inversion of seismic waveforms, *J. geophys. Res.*, **89,** 5953–5986.